Keysight Technologies
Three dimensional infinite-element simulations of a scanning microwave microscope cantilever for imaging at the nanoscale

Article Reprint

www.keysight.com
www.keysight.com/find/ict
www.keysight.com/find/contactus

KEYSIGHT
TECHNOLOGIES

Three-dimensional finite-element simulations of a scanning microwave microscope cantilever for imaging at the nanoscale

A. O. Oladipo, M. Kasper, S. Lavdas, G. Gramse, F. Kienberger, and N. C. Panoiu

Three-dimensional finite-element simulations of a scanning microwave microscope cantilever for imaging at the nanoscale

A. O. Oladipo,[1,2,a)] M. Kasper,[3] S. Lavdas,[2] G. Gramse,[3] F. Kienberger,[4] and N. C. Panoiu[2,5]

[1]Bio-Nano Consulting, 338 Euston Road, London NW1 3BT, United Kingdom
[2]Electronic and Electrical Engineering Department, University College London, Torrington Place, London WC1E 7JE, United Kingdom
[3]Biophysics Institute, Johannes Kepler University Linz, Gruberstrasse 40, 4020 Linz, Austria
[4]Agilent Technologies Austria GmbH, Gruberstrasse 40, 4020 Linz, Austria
[5]Thomas Young Centre, London Centre for Nanotechnology, University College London, 17-19 Gordon Street, London WC1H 0AH, United Kingdom

We use three-dimensional finite-element numerical simulations to fully characterize the electromagnetic interactions between a metallic nano-tip and cantilever that are part of a scanning microwave microscopy (SMM) system and dielectric samples. In particular, we use this rigorous computational technique to analyze and validate a recently developed SMM calibration procedure for complex impedance measurements in reflection mode. Our simulations show that relatively small changes in the conductivity of the substrates can cause significant variations in the measured reflection coefficient. In addition, we demonstrate that the bulk systemic impedance is extremely sensitive to modifications of system parameters, namely, variations in the cantilever inclination angle as small as 1° cause changes in system impedance that can be larger than 10%. Finally, the main experimental implications of these results to SMM imaging and calibration are identified and discussed. ⱽ 2013 AIP Publishing LLC. [http://dx.doi.org/10.1063/1.4832456]

The ability to observe and/or control nanoscale physical phenomena can be viewed as the backbone of most of the nanotechnology research conducted nowadays by scientist and engineers. The array of applications of nanotechnology continues to expand rapidly, with beneficiaries in electronics,[1–3] materials science,[4–6] biology,[7,8] medicine,[9] and other important segments of industry and society. As a result, the volume, complexity, and diversity of nano-samples that require imaging and characterization are ever increasing. To cope with such diversity of samples, it is becoming increasingly more pressing to develop fast, accurate, and versatile broadband microscopy techniques. Several such imaging techniques have been used to characterize the physical properties of materials and devices at different length scales. For example, optical and electron microscopes as well as atomic force microscope (AFM) have been used to obtain detailed structural and tomographic images of samples.[10,11] Furthermore, electrostatic force microscopy (EFM)[12–14] and scanning microwave microscopy (SMM)[15,16] techniques have been shown to accurately provide the local dielectric properties of materials at the nanoscale.

A unique feature of SMM is that it combines the high lateral sensitivity of AFM with the versatility, speed, and accuracy of vector network analyzers (VNA).[17,18] In the SMM transmission line technique from Agilent, the VNA generates a continuous microwave signal with a typical frequency of 1–20 GHz, which is forwarded to a conductive AFM tip. Depending on the electrical properties of the sample and the impedance between the tip-sample interfaces, part of the microwave signal is reflected and the ratio of the outgoing signal and reflected signal is measured by the VNA

as a scattering reflection signal, S_{11}. While SMM is commonly used in semiconductor industry for dopant profiling applications and in materials science for calibrated capacitance measurements, there are several limitations that currently are not fully addressed. For instance, the effect of varying AFM tip shape and tip-wearing during imaging, as well as the presence of non-local stray fields, complicate the quantitative analysis of the imaging process and limit the accurate calibration of the microscope.

Here, we use rigorous three-dimensional (3D) finite element modeling to characterize and improve the accuracy of SMM calibration and measurement analysis. Our work suggests that 3D finite-element method (FEM) modeling of the electromagnetic interaction between the tip and sample is a versatile technique that provides unique insights, which are instrumental when planning an experiment, and for understanding and validating experimental findings and calibrations as well. We determined the 3D electric field distribution of a SMM system in contact mode and investigated the effect of varying the conductivity of the bulk silicon substrate layer and inclination angle of the probe on the capacitance and resistance at the tip. In particular, our analysis clearly shows that an accurate quantitative description of the stray capacitance contributions from the cantilever and cone part of the probe, key quantities that are difficult to separate in an experimental setting, can be achieved only if 3D simulations techniques are employed. The sensitivity of the tip capacitance and resistance with variations in the operational frequency was also studied.

The calibration sample investigated in this study is schematically shown in Fig. 1(a). It comprises a relatively thick layer of doped silicon substrate ($h_{Si} = 500 \, \mu m$) on top of which a staircase layer with thickness, $h = 200 \, nm$, of SiO_2

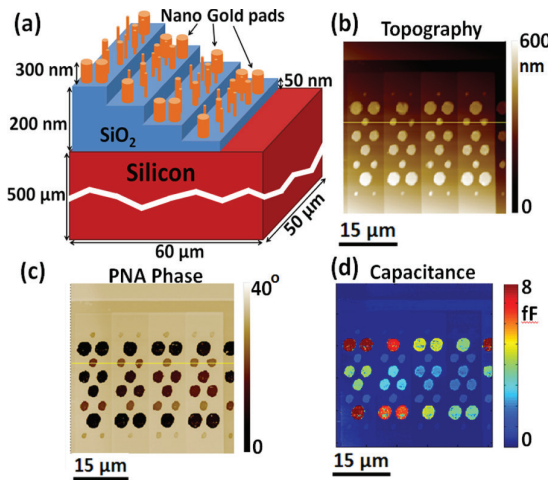a)Electronic mail: Abiola.Oladipo@bio-nano-consulting.com

FIG. 1. (a) A 3D schematic of the calibration sample, (b) topography image, (c) VNA phase image, and (d) the capacitance image of the sample which was obtained from the calibration algorithm.

FIG. 2. (a) A 3D model of a platinum AFM-type probe in contact with a calibration sample that consists of a gold-pad on a layer of SiO_2 (shown in the inset) all deposited on a bulk silicon substrate. The distribution of the electric field amplitude in the (b) longitudinal symmetry plane and (c) several transverse planes of the model.

was deposited. The thickness of each step in the SiO_2 layer was $h_{SiO_2} = 50$ nm. On each step of the SiO_2 layer, gold nano-pads with height, $h_{Au} = 300$ nm, and various diameters, $D = 11\,\mu m$; $D = 21\,\mu m$; $D = 61\,\mu m$, and $D = 101\,\mu m$ were deposited.

Figure 1(b) shows a topographical image of the calibration sample while the simultaneously acquired VNA phase image of the S_{11} coefficient is shown in Fig. 1(c) (SMM from Agilent Technologies, Chandler, USA). Using the three-point calibration algorithm from Ref. 19 (see also the discussion below), the calibrated capacitance image was calculated and plotted in Fig. 1(d). The aim of this calibration algorithm is to map the complete systemic reflection coefficient measured by the VNA, $S_{11,m}$, to the complex impedance at the tip, Z_{probe}, the relation between the two quantities being given by the following system of equations,

$$S_{11;probe} = \frac{S_{11;m} - e_{00}}{e_{01} + e_{11}S_{11;m}}; \tag{1a}$$

$$Z_{probe} = Z_{ref}\frac{1 + S_{11;probe}}{1 - S_{11;probe}}: \tag{1b}$$

Here, Z_{ref} is a reference impedance, and e_{00}, e_{01}, and e_{11} are calibration parameters. Therefore, three gold nano-pads on SiO_2 slabs of varying thickness were selected and used to generate the three complex coefficients, e_{00}, e_{01}, and e_{11}, required to construct a black-box transfer function. This is done by comparing the measured complex reflection coefficient, $S_{11,m}$, with the theoretical one, $S_{11,probe}$, and assuming that the impedance of the oxide is fully capacitive. It is also assumed that the capacitance can be calculated from the parallel plate formula.

In order to analyze numerically the calibration algorithm and validate the underlying assumptions we have computed numerically the theoretical values Z_{probe}, entering in Eq. (1). To this end, we performed a 3D finite-element analysis of the electromagnetic interactions at the SMM tip by using the EMPro, a commercially available software.[20] As illustrated in Fig. 2(a), our 3D model of the full SMM system includes
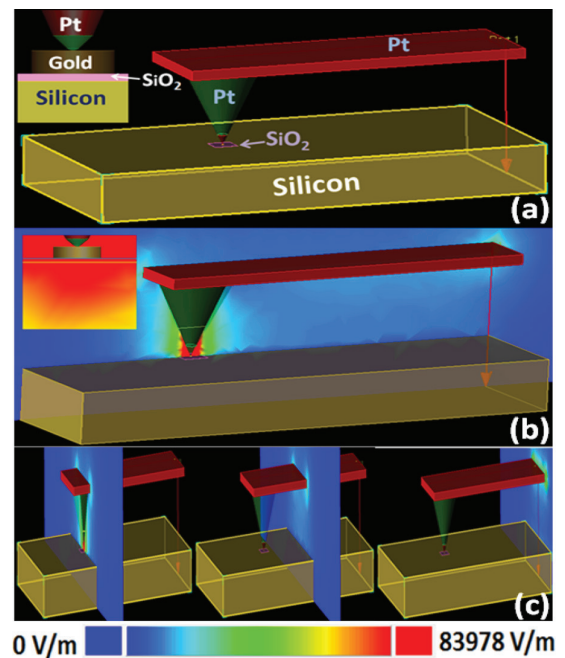
the complete bulk platinum AFM-type probe (cantilever and cone), which is in contact with the sample that is investigated (same as in the experiment). We show in Fig. 2(b) the cross sectional distribution of the electric field amplitude at the symmetry longitudinal plane along the length of the structure. As expected, the largest penetration depth of the electric field into the sample is seen in the region directly beneath the tip of the probe [see inset of Fig. 2(b)]. Furthermore, the electromagnetic interaction between the cantilever and the bulk silicon substrate indicates that the complete system impedance is a sum of the impedance at the tip and the impedance contributions from the cantilever and cone. Equally important, the field distribution in Figs. 2(b) and 2(c) suggests that 3D simulations are crucial for obtaining an accurate description of the system impedance. More specifically, it should be clear that this spatial distribution of the field, and consequently the corresponding stray capacitance, cannot be captured by 2D models that implicitly assume axial symmetry of the system.

In order to model a calibrated SMM system only the small radius, $R \simeq 100$ nm, nano-sphere at the very end of the metallic tip was considered, so as to avoid the stray field contributions from the cantilever and cone. The value of R is strongly related to the lateral resolution/sensitivity of the SMM. The entire computational domain was enclosed in a large air-box bounded by perfectly matched layers. The calibrated SMM model has a 10 GHz unit voltage applied to the nano-sphere relative to the ground, which is located at the bottom plane of the entire simulation domain. The tip capacitance, $C_{probe} = \frac{1}{2\pi f X_c}$, computed by using this procedure for gold-pad diameters ranging from $D = 1\,\mu m$ to $D = 10\,\mu m$ and for different conductivity of the bulk silicon substrate is

present in Fig. 3(a). In this analysis, X_c is the capacitive reactance at tip. At high conductivity values of the silicon substrate ($\sigma \gtrsim 100$ S=m) the substrate can be considered to be nearly metallic and as such the tip capacitance increases quadratically with the gold-pad diameter. However, when the conductivity of the silicon substrate is small ($\sigma \lesssim 10$ S=m), the tip capacitance increases linearly with the gold-pad diameter. This indicates that the dopant density of the substrate in the sample plays an important role in determining the value of the tip capacitance and should be well known in order to obtain a reliable calibration of the SMM system.

For the case where the conductivity of the silicon substrate is 100 S/m and above, which is used in the currently available SMM capacitance calibration samples, the plots in Fig. 3(b) suggest that there is a very good agreement between our 3D FEM modeling results and the experimental data obtained from the calibration algorithm. These results validate the three standard calibration algorithm described by Eq. (1). Also, we present in Figs. 3(b) and 3(c) the tip capacitance and resistance for varying gold-pad diameters and height of the SiO$_2$ layer. Specifically, the results summarized in Fig. 3(b) demonstrate that our 3D FEM analysis agrees fairly well with the analytical results obtained by using the parallel-plate capacitance formula, $C = \frac{\varepsilon A}{h}$, especially for oxide thickness $h = 50\,\mu$m. This confirms that the fringing field contributions to the tip capacitance are minimal, as conjectured in Ref. 19. However, since the substrate is not fully metallic, we also observe a resistive component
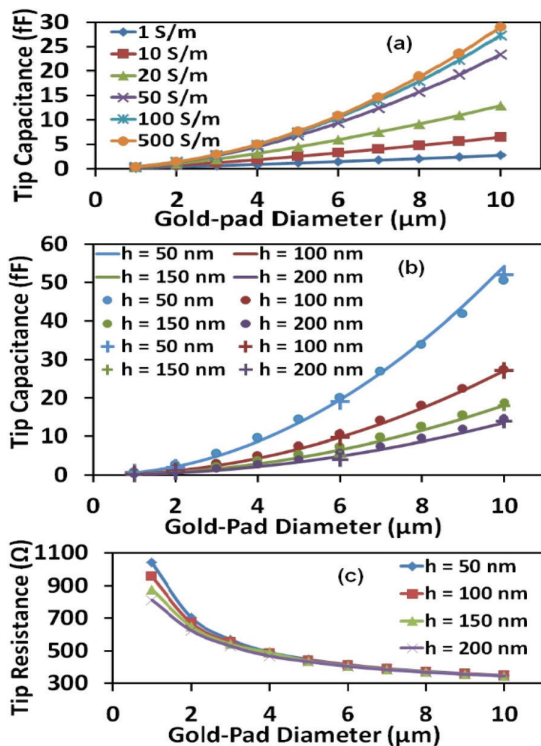
of the impedance that has to be considered in the calibration procedure. This resistance decreases with the gold-pad diameter and the height of SiO$_2$ layer.

In Fig. 4(a), we compare the complete system capacitance with the capacitance at the tip for 30 electrically different (gold-pad diameter and SiO$_2$ height) samples. We computed the stray capacitance induced by the cantilever by analyzing the SMM system as a network of lumped elements, with capacitors in parallel as shown in the inset of Fig. 4(b). Under this assumption, the capacitances in the system are related by $C_{\mathrm{stray}} = C_{\mathrm{system}} - C_{\mathrm{tip}}$. As it can be seen in Fig. 4(b), the average stray capacitance falls within the stray capacitance range for all values of the height of the SiO$_2$ layer. Also, we found that the range of the stray capacitance decreases with the height of the SiO$_2$ layer even though the maximum stray capacitance in each case was approximately the same. We also modelled the variation of the stray capacitance as the AFM probe approaches the sample [see the inset in Fig. 4(a)], a physical quantity that is closely related to the system sensitivity. Our calculations resulted in a stray capacitance variation of $\sim$0.025 aF/nm along the vertical direction, which is in the range of recent experimental measurements.[18]

In order to extend this calibration algorithm to the characterization of arbitrary samples, it is imperative to assess

FIG. 3. (a) Tip capacitance vs. the gold-pad diameter, calculated for different values of the silicon substrate conductivity. (b) Tip capacitance *vs.* the gold-pad diameter, determined for different h, from FEM (markers), analytical calculation (solid lines), and experiment (crosses). (c) Tip resistance *vs.* the gold-pad diameter, determined for different h.
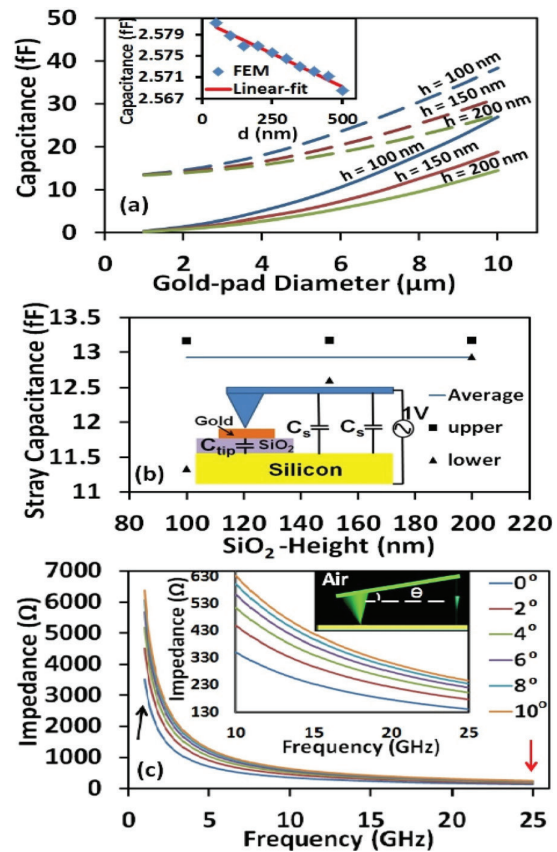

FIG. 4. (a) Comparison between the full system capacitance (dashed lines) and the capacitance at the tip (solid lines). In inset, the capacitance variation with the tip-sample distance at $h = 50$ nm and $D = 10$ nm. (b) Stray capacitance estimated as average over 30 samples. The thickness of the SiO$_2$ layer is $h = 100$nm, $h = 150$ nm, and $h = 200$ nm. (c) System impedance *vs.* frequency, determined for different inclination angles of the probe. The model schematics with inclined probe is shown in the inset.

the effect of variations during imaging, as illustrated schematically in Fig. 4(c). Here we outline in Fig. 4(c) the effect of varying the inclination of the cantilever and cone, on the bulk systemic impedance. We stress again that 3D simulations are essential for this analysis as the system does not possess axial symmetry. Our numerical simulations show that a 1° increase in the inclination angle causes about 10% increase in the total impedance. This finding suggests that even small changes in the scanning set point of the SMM could have a large impact on the measurement sensitivity after calibration. Thus, the imaging force and cantilever inclination angle are maintained constant. Equally important, we found out that at low frequencies (< 1 GHz) the resistive impedance R can be neglected [$X_c = 3519.57\,\Omega$; $R = 42.89\,\Omega$, black arrow in Fig. 4(c)], whereas at high frequencies (> 25 GHz) this approximation is no longer valid [$X_c = 134.11\,\Omega$; $R = 43.56\,\Omega$, red arrow in Fig. 4(c)].

In conclusion, we have performed a theoretical analysis and numerical validation of a calibration algorithm for SMM imaging at the nanoscale. We found good agreement between our computational results and the experimental data. In addition, our study revealed that even small variations in the conductivity of the silicon substrate can cause significant variation of the obtained calibration parameters. We also estimated the stray capacitance contributions from the cantilever and cone and found that the average stray capacitance falls within the stray capacitance range for different SiO_2 heights. We also demonstrated that the bulk systemic impedance is strongly sensitive to variations of the inclination angle of the cantilever. These conclusions have significant experimental implications, as they underline the importance of the sensitivity of a widely used SMM calibration procedure.

[1]E. Kymakis and G. A. J. Amaratunga, Appl. Phys. Lett. 80, 112 (2002).

[2]W. Zhu, C. Bower, O. Zhou, G. Kochanski, and S. Jin, Appl. Phys. Lett. 75, 873 (1999).

[3]B. T. Rosner and D. W. van der Weide, Rev. Sci. Instrum. 73, 2505 (2002).

[4]A. C. Balazs, T. Emrick, and T. P. Russell, Science 314, 1107 (2006).

[5]H.-Y. Chen, M. K. F. Lo, G. Yang, H. G. Monbouquette, and Y. Yang, Nat. Nanotechnol. 3, 543 (2008).

[6]M. M. van Schooneveld, A. Gloter, O. Stephan, L. F. Zagonel, R. Koole, A. Meijerink, W. J. M. Mulder, and F. M. F. de Groot, Nat. Nanotechnol. 5, 538 (2010).

[7]P. Alivisatos, Nat. Biotechnol. 22, 47 (2004).

[8]X. Michalet, F. F. Pinaud, L. A. Bentolila, J. M. Tsay, S. Doose, J. J. Li, G. Sundaresan, A. M. Wu, S. S. Gambhir, and S. Weiss, Science 307, 538 (2005).

[9]M. E. Davis, Z. Chen, and D. M. Shin, Nat. Rev. Drug Discovery 7, 771 (2008).

[10]D. M. Jones, J. R. Smith, W. T. S. Huck, and C. Alexander, Adv. Mater. 14, 1130 (2002).

[11]D. Fotiadis, S. Scheuring, S. A. Muller, A. Engel, and D. J. Muller, Micron 33, 385 (2002).

[12]L. Fumagalli, D. Esteban-Ferrer, A. Cuervo, J. S. Carrascosa, and G. Gomila, Nature Mater. 11, 808 (2012).

[13]S. Belaidi, P. Girard, and G. Leveque, J. Appl. Phys. 81, 1023 (1997).

[14]J. W. Hong, K. H. Noh, S. Park, S. I. Kwun, and Z. G. Khim, Phys. Rev. B 58, 5078 (1998).

[15]C. Gao, T. Wei, F. Duewer, Y. L. Lu, and X. D. Xiang, Appl. Phys. Lett. 71, 1872 (1997).

[16]M. Tabib-Azar and Y. Q. Wang, IEEE Trans. Microwave Theory Tech. 52, 971 (2004).

[17]H. Tanbakuchi, M. Richter, F. Kienberger, and H. P. Huber, in IEEE *International Conference on Microwave, Communication, Antennas and Electronics Systems, Tel Aviv, Israel, 2009*, pp. 1–4.

[18]H. P. Huber, M. Moertelmaier, T. M. Wallis, C. J. Chiang, M. Hochleitner, A. Imtiaz, Y. J. Oh, K. Schilcher, M. Dieudonne, J. Smoliner, P. Hinterdorfer, S. J. Rosner, H. Tanbakuchi, P. Kabos, and F. Kienberger, Rev. Sci. Instrum. 81, 113701 (2010).

[19]J. Hoffmann, M. Wollensack, M. Zeier, J. Niegemann, H. Huber, and F. Kienberger, in *12th IEEE International Conference on Nanotechnology, Birmingham, UK, 2012*, pp. 1–4.

[20]EMPro 3D EM Simulation Software, Agilent Technologies, Inc.

5991-3789EN